

Restructuring of MFI Framework Zeolite Models and Their Associated Artifacts in Density Functional Theory Calculations

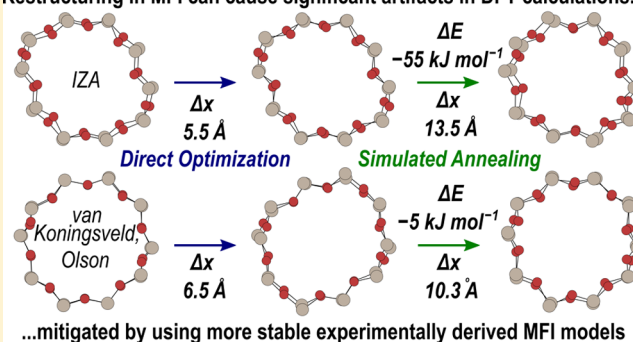
Alexander Hoffman,¹ Mykela DeLuca, and David Hibbitts*¹

Department of Chemical Engineering, University of Florida, Gainesville, Florida 32601, United States

Supporting Information

ABSTRACT: This study compares and evaluates multiple orthorhombic silicalite MFI framework structures using periodic density functional theory (DFT) calculations implemented with a wide range of exchange–correlation functionals and dispersion-correction schemes. Optimization of the structure available from the International Zeolite Association (IZA) yields only metastable forms, which restructure to arrangements 18–156 kJ mol⁻¹ lower in energy (55 kJ mol⁻¹ on average) through annealing and adsorption/desorption processes without altering their connectivity. These restructuring events can occur unintentionally during DFT studies of adsorptive and catalytic properties, leading to very large artifacts in DFT-predicted adsorption, reaction, and activation energies. Pre-annealing the IZA structure prevents restructuring and these artifacts but forms MFI structures which do not conform to the *Pnma* spacegroup symmetry and have significantly perturbed sinusoidal and straight channel geometries. These issues persist across a wide range of exchange–correlation functionals, including common choices such as the Perdew–Burke–Ernzerhof and Bayesian error estimation functionals, and dispersion-correction schemes such as the D3 method. Direct optimization of structures generated from the work of van Koningsveld et al. and Olson et al., in contrast, yields structures that are extremely similar across all functionals, restructure less often during annealing, and have smaller energy shifts when they do restructure (5 kJ mol⁻¹, on average). Optimizing the unit cell parameters of these structures without constraining atoms or the unit cell shape also yields more stable structures, though often with unit cell parameters that do not closely match structures found experimentally. Annealing of other commonly studied zeolites (BEA, CHA, and LTA) does not yield structures with energy decreases or structural changes as significant as those for MFI. This study thus illuminates a potential source of significant error for DFT studies of MFI and provides evidence-based solutions for a variety of DFT methods.

Restructuring in MFI can cause significant artifacts in DFT calculations...



1. INTRODUCTION

Zeolites are microporous aluminosilicates that are important in industrial and academic applications, including separations processes,^{1–5} catalytic cracking,^{6–11} and biomass conversion.^{12–20} Zeolites stabilize adsorbed guest species in their pores through noncovalent interactions (e.g., dispersive, electrostatic, H-bonding),^{21–26} which depend on the size and shape of the zeolite pores.²⁷ Over 200 zeolite frameworks have been synthesized^{28–30} and more than 350 000 others are theoretically stable materials and thus potential synthesis targets;^{31,32} despite the large number of available frameworks, the MFI framework is ubiquitous in processes that require zeolite catalysts or molecular sieves.³³ MFI has two distinct 10-member ring (10-MR) channels: one straight and one sinusoidal, which intersect to form larger voids. These structural properties make MFI a shape-selective catalyst and separation material. Furthermore, MFI is stable at a wide range of temperatures (up to at least 800 K),³⁴ making it an ideal catalyst for broad applications.

Density functional theory (DFT) is commonly employed to analyze sorptive^{28,35–44} and catalytic properties^{22,45–59} of

zeolites, including MFI.^{40,42,43,59–78} Many different exchange–correlation functionals are used in zeolite-related DFT studies; however, dispersive and van der Waals forces are not internally accounted for in most DFT functionals, a correction which is important for energy calculations in zeolites as micropores of MFI stabilize guest species through dispersive and van der Waals interactions.^{21–23,26,48} These interactions can be included in calculations within an exchange–correlation functional—e.g., the van der Waals density functional (vdW-DF2)^{79,80}—or by using empirically fitted adjustments to energies calculated with functionals that do not internally account for these interactions—e.g., combining the Perdew–Burke–Ernzerhof (PBE)⁸¹ functional with Grimme’s DFT-D3 dispersion correction with Becke–Johnson damping (D3BJ).^{82,83} Many of these different functional schemes are used in DFT analyses of the properties of MFI zeolites, the most common of which is the PBE functional,^{54,59} often with Grimme’s dispersion correc-

Received: December 20, 2018

Revised: February 9, 2019

Published: February 15, 2019

tion.^{42–44,63,73–77} Previous work has indicated that dispersion-corrected DFT calculations more accurately model unit cell sizes of Si-form zeolite structures.^{84–87}

There are three orthorhombic crystal structures that are commonly used as source structures for DFT calculations of the MFI framework: one provided by the International Zeolite Association (IZA) database (IZA-DLS76),⁸⁸ one published by Olson et al. (1981) from X-ray diffraction of a ZSM-5 structure with a Si/Al ratio near 90 (Olson-Ortho),⁸⁹ and one published by van Koningsveld et al. (1990) from X-ray diffraction measurements of a high-temperature-treated MFI framework zeolite (vK-HT-Ortho; Si/Al \approx 300).⁹⁰ These MFI structures are all orthorhombic with the *Pnma* spacegroup symmetry, and their cell parameters are summarized in Table 1. Each

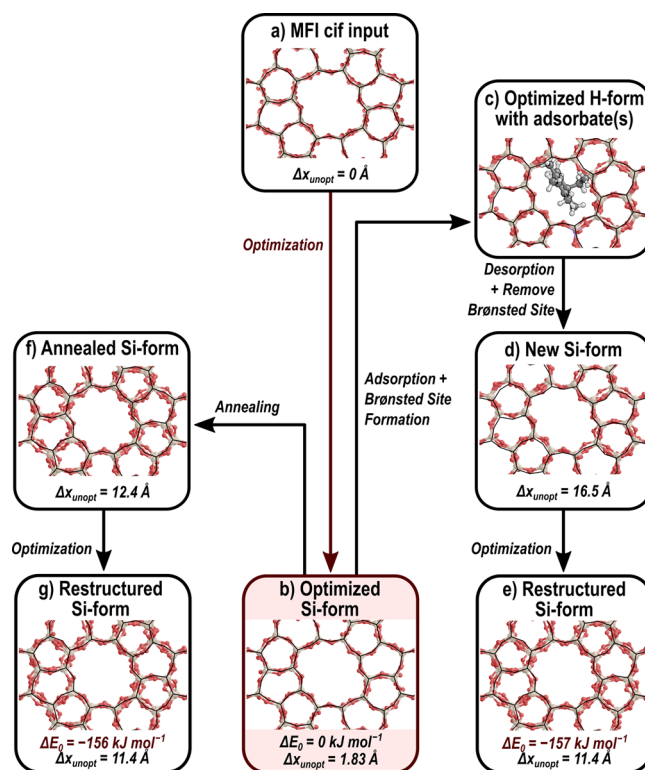
Table 1. Origins and Framework Unit Cell Parameters for Each of the Tested Frameworks in This Work

source	Si/Al	<i>a</i> , <i>b</i> , <i>c</i> (Å)
IZA-DLS76	N/A	20.090, 19.738, 13.142
Olson-Ortho	90	20.07, 19.92, 13.42
vK-HT-Ortho	300	20.078, 19.894, 13.372

framework contains 96 tetrahedral Si atoms (T-sites) and 192 O atoms in its unit cell. The IZA-DLS76 structure is most commonly deployed among theoretical investigations of the properties of MFI zeolites.

Here, we document how these three MFI source structures (IZA-DLS76, Olson-Ortho, and vK-HT-Ortho) are unstable in many common exchange–correlation functionals and dispersion-correction schemes. Optimization of these structures results in metastable frameworks. These can restructure into more stable forms during DFT studies of their catalytic and sorptive properties, resulting in significant artifacts affecting the predictions of relevant adsorption and reaction energies. These restructuring events can occur through perturbation associated with adsorption of guest species or through *ab initio* molecular dynamic simulated annealing calculations. Scheme 1 outlines an example of this restructuring for the IZA-DLS76 structure. Direct optimization yields a local minimum structure which is similar to the original unoptimized structure; the formation of a Brønsted acid site and the adsorption of a methylbenzene intermediate (Scheme 1c), however, sufficiently perturbs the framework to allow it to access an MFI structure 157 kJ mol^{−1} more stable than the directly optimized structure upon removal of the adsorbate and Brønsted acid and subsequent re-optimization (Scheme 1e). Similarly, simulated annealing of the directly optimized structure followed by re-optimization yields an essentially identical structure (Scheme 1g) that is 156 kJ mol^{−1} more stable than the directly optimized structure. These restructuring events are not consistent during adsorption and reaction modeling and thus can cause severe artifacts in the calculation of adsorption, activation, and reaction energies by DFT methods. The stability of directly optimized MFI structures differs for all three MFI source structures and across all DFT methodologies used herein. Energy barriers to transition from one MFI structure to another were calculated to be less than 85 kJ mol^{−1}, indicating that these restructuring events are likely to occur at reaction conditions providing further evidence of the flexibility of the framework to modify its local structure near guest species. The artifacts associated with these transformations can be mitigated by pre-annealing MFI in the DFT methodologies of the study to obtain a more stable structure

Scheme 1. Formation of Different Si-Form Structures with MFI Connectivity Starting with the IZA-DLS76 Structure Using the RPBE Exchange–Correlation Functional and the DFT-D3 Dispersion Scheme^a



^aAdsorbates and simulated annealing can allow the surrounding framework to overcome barriers and escape local minima to restructure, resulting in more stable Si-forms.

which is less likely to subsequently restructure and thus will provide a more consistent catalyst model for all adsorption and reaction modeling calculations.

2. METHODS AND INPUT STRUCTURES

2.1. Computational Methods. Periodic planewave DFT calculations were performed using the Vienna *ab initio* software package (VASP).^{91–94} Planewaves were constructed using the projector-augmented wave method.⁹⁵ The energy cutoff for optimizations was 400 eV for calculations which did not vary the unit cell parameters and 800 eV for those that allowed the unit cell size to vary. Atomic positions were optimized such that the forces on each atom were <0.01 eV Å^{−1} and no atoms were constrained during these optimization calculations. Several exchange–correlation functionals were compared within this work: the PBE functional,⁸¹ the revised PBE functional (RPBE),⁹⁶ the optB86b and optPBE functionals that internally account for van der Waals forces,^{97,98} the updated van der Waals density functional (vdW-DF2),^{79,80} the Perdew–Wang 91 functional (PW91),^{99,100} the reviewed PBE with internal vdW correction (revPBE-vdW),^{101,102} the PBE functional revised for solids (PBEsol),^{103,104} and the Bayesian error estimation functional (BEEF).^{41,105} Structures optimized using the RPBE and PBE functionals were optimized with and without DFT-D3 dispersion correction with Becke–Johnson damping (D3BJ),^{82,83} denoted as RPBE-D and PBE-D. The Brillouin zone was sampled at the Γ -point for all calculations. The PBE functional remains the most common functional for analysis of

MFI properties, though the newer BEEF functional—which internally accounts for noncovalent interactions—is growing in use. Generic comparisons across a wide set of properties indicate that RPBE is more accurate than PBE for nonspecific applications¹⁰⁶ and more accurately captures H-bonding behavior of adsorbates in zeolites.¹⁰⁷ All energies reported here are electronic energies (E_0) and are reported for entire MFI unit cells (i.e., total energies for all 96 tetrahedral units of the MFI unit cell, not normalized per tetrahedral unit), unless otherwise noted.

Unit cell parameters were optimized for each MFI source structure (Table 1) with each functional and dispersive correction scheme examined here (Table 2). Unit cell

Table 2. Exchange–Correlation Functional and Dispersive Correction Schemes Tested

functional	dispersive correction
BEEF	internal
RPBE	none, D3BJ
PBE	none, D3BJ
PBEsol	none
optPBE	internal
revPBE-vdW	internal
optB86b	internal
vdW-DF2	internal
PW91	none

parameters were optimized both with and without concurrent shape relaxation and with and without concurrent relaxation of the atomic coordinates (settings 3, 6, and 7 of VASP's ISIF parameter). An energy cutoff of 800 eV was used for all unit cell

parameter optimization calculations and were electronically converged (instead of a force convergence) such that energies calculated between iterations differed by $<1 \times 10^{-6}$ eV.

Periodic ab initio molecular dynamics (AIMD) calculations were used to simulate annealing of each MFI source structure (Table 1) in each functional (Table 2). Structures were annealed from 200 to 800 K over 3 ps, held at 800 K for 3 ps, and cooled from 800 to 100 K for 15 ps. A timestep of 3 fs was used for all AIMD calculations. Following the cooling step, the final structure from the simulated annealing was optimized such that the forces on each atom were <0.01 eV \AA^{-1} , similar to all other optimizations.

The nudged elastic band (NEB) method was used to approximate barriers associated with restructuring the MFI framework.^{108,109} The NEB method used 16 images and converged structures to <0.1 eV \AA^{-1} .

2.2. Input Structures. MFI structures were obtained from the IZA database (IZA-DLS76),⁸⁸ recreated from the experimental results of Olson et al. (Olson-Ortho),⁸⁹ and from the experimental results of van Koningsveld et al. (vK-HT-Ortho).⁹⁰ The IZA-DLS76, Olson-Ortho, and vK-HT-Ortho structures are shown in Figure 1. While these structures share the same symmetry rules, the atomic positions and unit cell parameters differ slightly. The a unit cell vectors of the three structures differ by ≤ 0.02 \AA across all three forms but the b and c vectors vary by 0.18 and 0.28 \AA between IZA-DLS76 (shortest b and c vectors) and Olson-Ortho (longest b and c vectors). The straight pore of IZA-DLS76 is elliptical (minimum and maximum T–T site distances of 8.31 and 9.78 \AA , a ratio of 1.18; Figure 1) while the pores of the Olson-Ortho and vK-HT-Ortho structures are nearly circular (maximum T–T distance of 9.33 \AA for both structures and minimum distances of 8.98 and

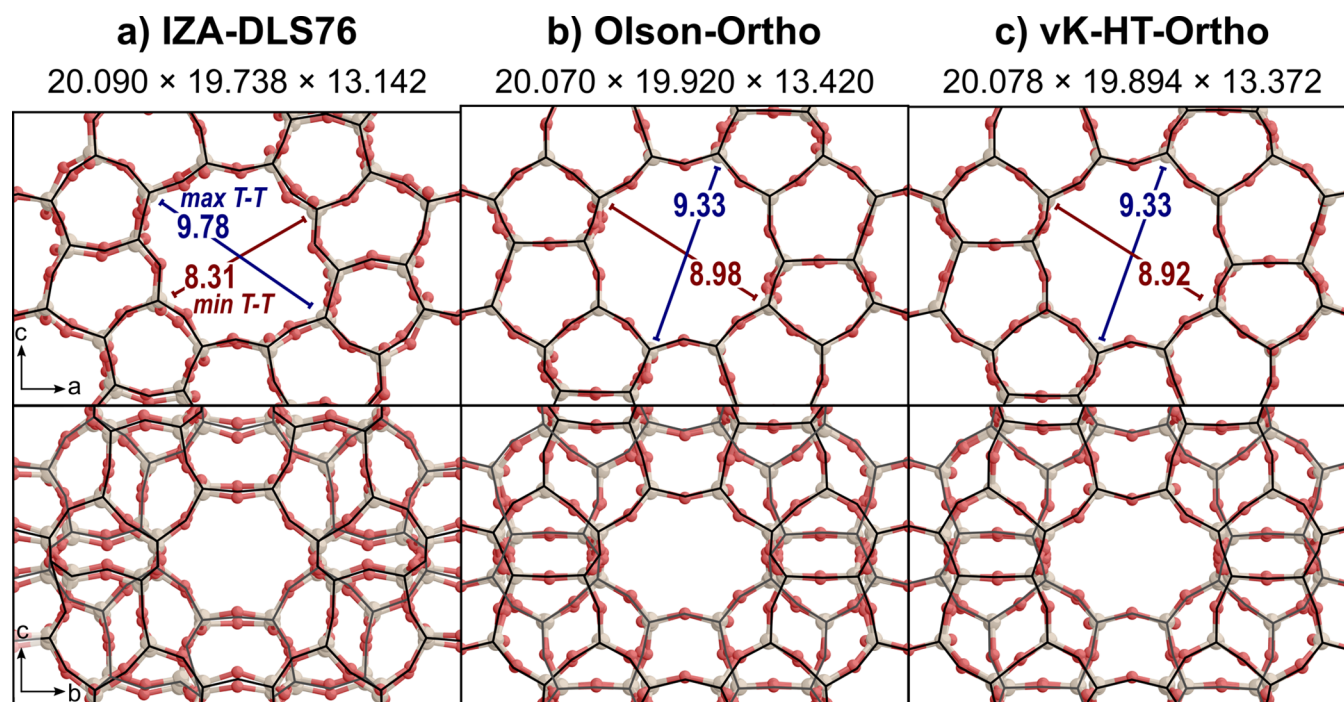


Figure 1. MFI structures from (a) IZA database (IZA-DLS76),⁸⁸ (b) experimental results of Olson et al. (Olson-Ortho),⁸⁹ and (c) experimental results of van Koningsveld et al. (vK-HT-Ortho).⁹⁰ The top row shows the view down the straight channel of MFI (along the b vector or $[010]$) and the bottom image shows a view down the sinusoidal channel (along the a vector or $[100]$). Each view is centered along the central axis of the respective channel. The lengths of the a , b , and c unit cell vectors for each structure are shown below in \AA . The maximum (blue) and minimum (red) distances between T-sites across the straight pores of each structure are also shown below in \AA .

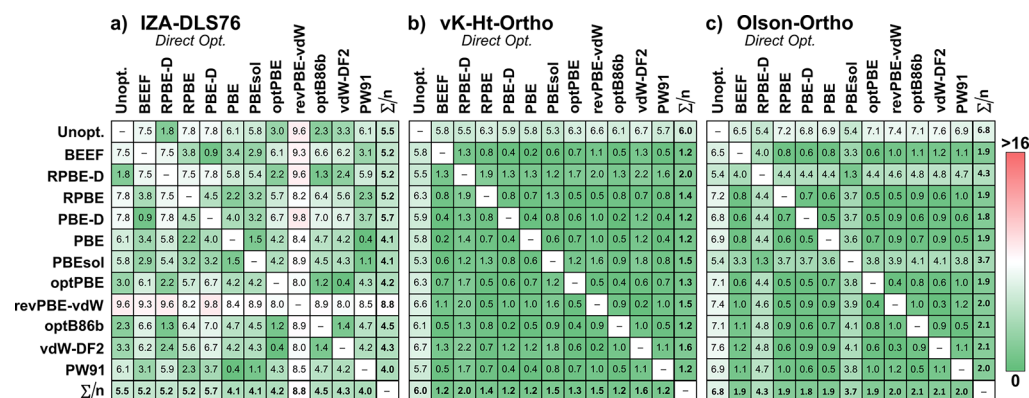


Figure 2. Calculated 3N-dimensional distances between (a) the initial IZA-DLS76 structure, (b) the initial vK-HT-Ortho structure, and (c) the initial Olson-Ortho structure and the structures for each found by optimization in each tested functional. The rightmost column and bottom row (Σ/n) show the average distance between the optimized structure from each functional and those from all other functionals and the unoptimized structure.

8.92 Å, a ratio of 1.04 for both; Figure 1). The optimization method used to create the IZA-DLS76 structure led to some disorder in the framework compared to the experimental source structures (Figure 1). Additionally, a $2 \times 2 \times 2$ supercell of α -quartz (unit cell parameters $a = b = 10.056$ Å, $c = 11.038$ Å, $\alpha = \beta = 90^\circ$, $\gamma = 120^\circ$) was optimized in each of the above functionals.

2.3. Quantifying Structural Differences for MFI with Identical Unit Cell Parameters. A 3N-dimensional distance (Δx_{3N}) can be used to quantify the difference between two structures with identical unit cell parameters. This value can be used to quantify structural similarity but does not convey detailed information about structural differences. A 3N-dimensional distance between two structures (Δx_{3N}) is calculated by

$$\Delta x_{3N} = \sqrt{\sum_{i=1}^N (x_i - x'_i)^2 + (y_i - y'_i)^2 + (z_i - z'_i)^2} \quad (1)$$

where x_i , y_i , and z_i are the coordinates in Å of atom i in the unit cell of one structure and x'_i , y'_i , and z'_i are the coordinates of atom i in the second structure.

Similar or identical structures have identical energies; therefore, below a threshold value of Δx_{3N} , MFI structures can be considered equivalent despite slight structural differences. To determine this cutoff distance for uniqueness, a total of 10 877 structures were optimized with a Brønsted acid site at the T11 position in MFI and adsorbates from the methanol-to-olefin (MTO) processes (e.g., methylbenzenes, methanol, and dimethyl ether) in IZA-DLS76. The MFI framework underwent structural changes associated with the formation of a Brønsted acid site and addition of an adsorbate during these MTO-related calculations. Subsequently, Si-forms for each structure were generated by removing the Brønsted acid site and adsorbates without altering the location of any framework atoms. The 3N-dimensional distance was calculated between each structure; groups of structures separated by <2.0 Å were considered equivalent, leaving 2122 structures, which were then optimized to give a set of structures with MFI connectivity and their associated energies. The results of these calculations were then compared to determine how structural similarity (defined by Δx_{3N} distances) informed energy differences. Nearly all structural pairings (96.2%) with $\Delta x_{3N} < 3$ Å had energies within 5 kJ mol^{-1} of each other, and essentially all (99.9%) pairings with $\Delta x_{3N} < 3$ Å had energies within 10 kJ mol^{-1} of each other (see Table S1, Supporting Information). Structures with $\Delta x_{3N} > 3$ Å

of one another had energy differences of 0 – 157 kJ mol^{-1} , without a significant correlation within this range, as expected because two very different structures can have similar energies. Therefore, a cutoff distance of 3.0 Å appears reasonable to determine structural uniqueness, as structures within this 3N-distance of one another have extremely similar energies. All structures within the cutoff distance of one another ($\Delta x_{3N} < 3.0$ Å) were considered equivalent structures, leading to a total of 25 “unique” structures after optimization of the 2122 Si-form MFI structures. These 25 structures were optimized in each of the exchange–correlation functional schemes used here (Table 2).

This 3N distance can also be used to calculate deviation from the symmetry that may occur during optimization and restructuring events. Optimized structures can be used to generate symmetric structures by selecting one of each unique atom (T-site and O-site) in the output structure and applying the symmetry rules for MFI to generate the theoretical locations of the remaining atoms in MFI. The resulting 3N-dimensional distance between the optimized structure and the symmetric structure (Δx_{sym}) thus gives an indication as to how closely a structure that was optimized free of any constraints still conforms to the $Pnma$ spacegroup symmetry.

3. RESULTS AND DISCUSSION

3.1. Optimization of MFI Source Structures in Different Functionals. Optimizing the atomic positions of the three MFI source structures (Table 1, Figure 1) leads to different output structures in each functional examined in this work (Table 2). Relative Δx_{3N} values illustrate the amount of structural change between the input structures and their outputs after optimization in each functional. The relative deviations of the optimized IZA-DLS76 from the unoptimized structure are shown in Figure 2a. Optimization with RPBE-D alters the input structure the least ($\Delta x_{3N} = 1.83$ Å, indicating no significant change) while optimization in revPVE-vdW alters the input structure the most ($\Delta x_{3N} = 9.60$ Å) among the tested functionals. The revPBE-vdW functional optimizes IZA-DLS76 most differently from all other functionals, with an average distance from the other structures of 8.82 Å. These optimizations of the IZA-DLS76 structure lead to four categories of structures within which 3N-distances between structures are <3 Å. Optimized structures from the RPBE-D, optB86b, optPBE, and vdW-DF2 methods are similar to one another (Figure 3a), as are results from PBE-D and BEEF (Figure 3b) and results from RPBE, PBE, and PW91 (Figure

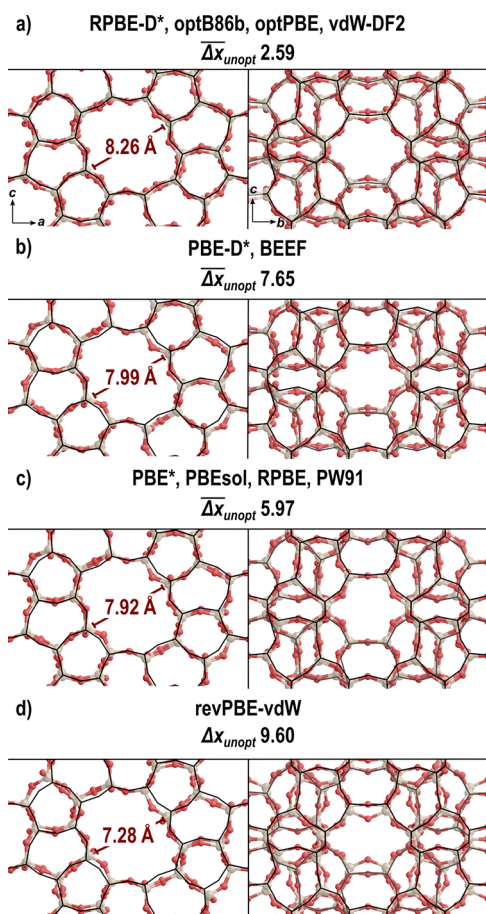


Figure 3. Structures after direct optimization of the IZA-DLS76 structure from (a) the grouping of RPBE-D, optB86b, optPBE, and vdW-DF2; (b) PBE-D and BEEF; (c) the grouping of RPBE, PBE, PBEsol, and PW91; and (d) revPBE-vdW. The functional used to optimize the structure shown for each group is denoted with an asterisk (*). The average distance from the input structure ($\overline{\Delta x}_{\text{ounopt}}$) is shown in Å for each grouping. The minimum distance between T-sites of the straight pore is shown for each structure in Å. All directly optimized IZA-DLS76 structures are shown in Figure S2 in the Supporting Information.

3c); the output of revPBE-vdW (Figure 3d) is dissimilar to those of all other exchange–correlation functionals. Each of these categories of outputs differs in their pore shapes and sizes (Figure 3). RPBE-D, optB86b, optPBE, and vdW-DF2 do not alter the IZA-DLS76 structure more than 3.5 Å during optimization. Upon optimization with revPBE-vdW, the straight pore narrows, forming a more elliptical shape, decreasing the minimum distance between T-sites across the straight pore from 8.31 to 7.28 Å (Figure 3d). Similar narrowing occurs during optimization in all other methods considered, albeit less severely (Figure 3a–c).

The 3N-distance between the RPBE and RPBE-D optimizations of the IZA-DLS76 structure is 7.53 Å, indicating a significant difference between the two outputs is caused by the inclusion of the DFT-D3 dispersion-correction method (Figure 2a). Inclusion of dispersive forces with the PBE functional does not result in differences as large as those for the RPBE functional. Furthermore, both the PBE and PBE-D outputs change significantly from the source IZA-DLS76 structure, whereas the RPBE optimization changes the input structure significantly

(7.76 Å), but RPBE-D is very similar to the unoptimized IZA-DLS76 source.

The vK-HT-Ortho and Olson-Ortho structures exhibit extremely similar behavior across all functionals tested during optimization (Figure 2b,c). For each of these inputs, the optimized structure deviated significantly ($\Delta x_{3N} > 5.4$ Å) from the MFI source structure, unlike the IZA-DLS76 optimizations. For the vK-HT-Ortho structure, the outputs of each functional differed by <2.2 Å from the outputs of other functionals, indicating that optimization of the vK-HT-Ortho structure resulted in approximately the same structure regardless of the DFT method (see Figure S3 in the Supporting Information for images of these structures). Similarly, optimized structures for the Olson-Ortho structure did not deviate significantly ($\Delta x_{3N} < 3.0$ Å) across functionals, except for the RPBE-D and PBEsol functionals, whose structures differ from other functionals by an average of 4.0 Å and are equivalent (see Figure S4 in the Supporting Information for images of structures).

The IZA-DLS76 MFI source behaves differently than the vK-HT-Ortho and Olson-Ortho structures. Direct optimization of IZA-DLS76 results in a variety of optimized structures depending on the exact functional and dispersion-correction scheme used in contrast to the relative structural indifference of the other MFI source structures.

Despite these structural deviations from the input structures, the optimized structures in each functional maintain the symmetry of the *Pnma* spacegroup; Δx_{sym} values are less than 0.005 Å for all directly optimized IZA-DLS76, vK-HT-Ortho, and Olson-Ortho structures. This indicates that the forces on each atom during direct optimization remain symmetric. These optimization calculations obtain local minima, however, which may not be global minima for MFI. After optimization, the MFI structure can be perturbed in two ways to yield Si-forms of energies that deviate from these directly optimized structures: through simulated annealing or through a pathway involving the adsorption of guest species (Scheme 1). Simulated annealing allows restructuring barriers to be overcome and new MFI forms to be found for each MFI source structure by simulating framework movement at high temperatures. The adsorption restructuring pathway changes the energy landscape by introducing an Al and proton to the framework and by the addition of guest species, which interact with the surrounding framework. The framework adjusts to accommodate guest species, which allows for restructuring barriers to be overcome. After desorption and removal of the added Brønsted acid site, MFI forms of differing stabilities can be found by optimizing the resulting Si-form.

3.2. Restructuring in MFI via Guest Species. New forms of the MFI framework were found by optimizing an H-form (Si/Al = 95) MFI in the presence of an adsorbate, followed by the removal of the Brønsted acid site and that adsorbate (Scheme 1c–e). Zeolite frameworks move to accommodate guest species; upon desorption, reversion to the Si-form, and subsequent optimization, the zeolite should return to the original framework structure. In cases described here, however, a more favorable form resulted from these framework alterations as predicted by these DFT methods. Notably, this is not adsorbate-forced restructuring; the initial Si-form of the MFI framework is inherently unstable, and the movement to accommodate any guest species allows for the framework to overcome the barrier required for framework atoms to shift to more stable positions.

If these restructuring events occur when guest species are in an unstable form of the MFI framework, they can lead to artifacts

that distort energies and structures. For example, restructuring can occur during optimization of the reactants, transition state, or products during calculations of reaction and activation energies; Figure 4 shows an example of artifacts we observed that

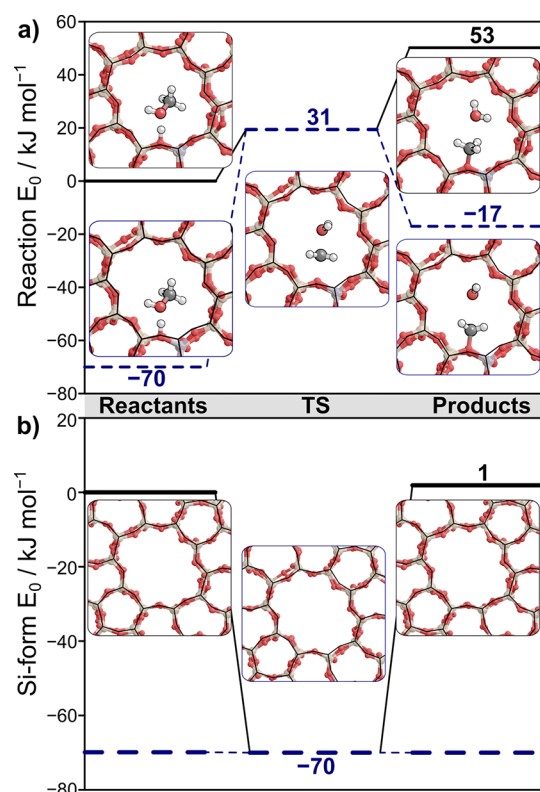


Figure 4. Reaction coordinate diagram that illustrates artifacts that can result from restructuring with adsorbate species in the IZA-DLS76 framework with RPBE-D. (a) Electronic energies (E_0) of the reactants, transition state, and products for surface methylation in MFI and (b) energies of the underlying Si-forms of the framework for each calculation. Calculations in restructured frameworks are in blue and those in frameworks that optimized to the same form as the optimized IZA form are in black.

resulted from restructuring induced by a transition state species during surface methylation in MFI, where restructuring leads to a false low barrier (and negative reverse barrier) because of a reduction in the energy of the surrounding framework. The restructuring decreased the relative energy of the MFI framework by 70 kJ mol⁻¹ for the transition state relative to the reactants or products which did not significantly restructure. The calculated ΔE_{act} appears to be 31 kJ mol⁻¹ when it is 101 kJ mol⁻¹; similarly, the reverse barrier appears to be negative (−22 kJ mol⁻¹) because of this artifact.

Restructuring in IZA-DLS76 was further examined by creating Si-form structures out of 10 877 optimized H-form structures related to the MTO process; of these, 2122 were optimized and analyzed, yielding 25 unique structures (see Section 2.3 for more details). These 25 unique structures were optimized in all DFT methods examined here (Table 2). Of those, we compare here the most stable structures for each functional. The functionals tested yield three groupings of structures that are considered most stable by each functional: (1) that favored by RPBE-D; (2) that favored by PBE-D, optB86b, and PW91; and (3) the structure favored by RPBE, PBE, PBEsol, optPBE, vdW-DF2, revPBE-vdW, and BEEF

(Figure 5). Structural distances outside of these groupings are >10 Å in all cases, indicating these three groups of structures are

IZA-DLS76
Post-Ads Opt.

	Unopt.	BEEF	RPBE-D	RPBE	PBE-D	PBE	PBEsol	optPBE	revPBE-vdW	optB86b	vdW-DF2	PW91	Σ/n
Unopt.	-	11.1	11.4	11.9	11.2	11.3	11.0	11.4	11.8	11.2	11.9	11.3	11.4
BEEF	11.1	-	12.2	1.2	17.2	0.6	0.7	0.6	1.0	17.2	1.2	17.4	7.3
RPBE-D	11.4	12.2	-	13.0	12.0	12.4	12.0	12.5	12.9	12.1	13.1	12.2	12.4
RPBE	11.9	1.2	13.0	-	18.2	0.9	1.6	1.4	0.9	18.2	0.8	18.4	7.8
PBE-D	11.2	17.2	12.0	18.2	-	17.4	16.9	17.5	18.0	0.3	18.1	0.6	13.4
PBE	11.3	0.6	12.4	0.9	17.4	-	0.6	0.9	0.9	17.4	0.9	17.6	7.4
PBEsol	11.0	0.7	12.0	1.6	16.9	0.6	-	1.1	1.5	16.9	1.5	17.1	7.4
optPBE	11.4	0.6	12.5	1.4	17.5	0.9	1.1	-	0.7	17.5	1.0	17.7	7.5
revPBE-vdW	11.8	1.0	12.9	0.9	18.0	0.9	1.5	0.7	-	18.1	0.4	18.3	7.7
optB86b	11.2	17.2	12.1	18.2	0.3	17.4	16.9	17.5	18.1	-	18.2	0.9	13.5
vdW-DF2	11.9	1.2	13.1	0.8	18.1	0.9	1.5	1.0	0.4	18.2	-	18.4	7.8
PW91	11.3	17.4	12.2	18.4	0.6	17.6	17.1	17.7	18.3	0.9	18.4	-	13.6
Σ/n	11.4	7.3	12.4	7.8	13.4	7.4	7.4	7.5	7.7	13.5	7.8	13.6	-

0 █ █ >16

Figure 5. Calculated 3N-dimensional distances between the input IZA-DLS76 structure and the most stable structure in each functional found by adsorbate-facilitated restructuring. The rightmost column and bottom row (Σ/n) show the average distance between the optimized structure from each functional and those from all other functionals and the unoptimized IZA-DLS76 structure.

very different from one another. The structure found through restructuring through this pathway with RPBE-D is totally unique, both from the input form and from the outputs of all other functionals, as the distances between its output and all other structures are >11 Å (Figure 5).

The output from RPBE-D shows disordering in its pore characteristics (Figure 6a), such that atoms that were aligned or nearly aligned in the initial IZA-DLS76 structure are no longer ordered. The outputs from the remaining functionals share similar characteristics, despite the uniqueness of the two groupings. Both the grouping from PBE-D, optB86b, and PW91 and the grouping from RPBE, PBE, PBEsol, optPBE, vdW-DF2, revPBE-vdW, and BEEF cease to have straight pores after restructuring has occurred, but instead the straight pore has deformed to yield two different regimes along the b vector (Figure 6b,c). In these structures, the major axis of the ellipse formed by the MFI pore changes directions, creating a pseudo-sinusoidal regime. After the framework restructures subsequent to adsorption/desorption, it no longer retains the $Pnma$ spacegroup symmetry (all structures have $\Delta x_{\text{sym}} > 8 \text{ \AA}$), and these deviations from the symmetry are apparent in the relative disorder in the straight pore of the RPBE-D optimized structure (Figure 6a) and in the sinusoidal views of the other structures (Figure 6b,c).

The structures produced from this analysis have large ranges in energy (Figure 7). The energy spread for the structures optimized by vdW-DF2 is the largest (181 kJ mol⁻¹) and is smallest in optB86b (123 kJ mol⁻¹). Critically, each scheme tested here shows many local minima with MFI connectivity but with energy spreads of >100 kJ mol⁻¹. If this adsorbate-facilitated restructuring occurs unexpectedly, reactant, product, and transition state energies could be incorrectly calculated (Figure 4). For most functionals, several unique structures exist within 20 kJ mol⁻¹ of the most stable structure found by facilitating restructuring with adsorbates; restructuring between

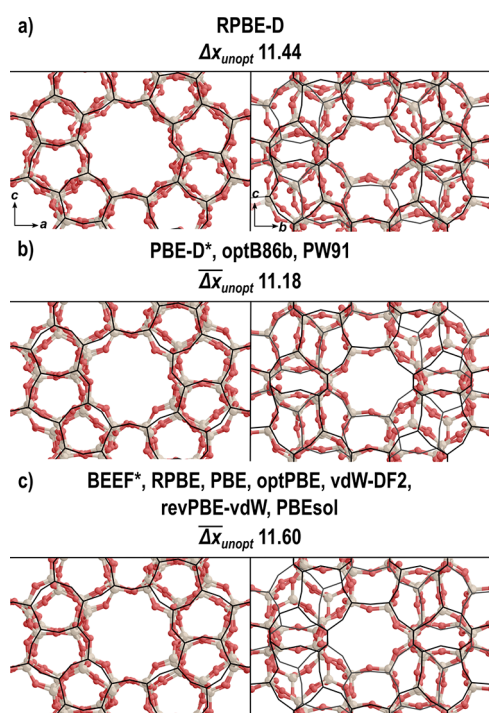


Figure 6. Structures after addition and removal of guest species to restructure the IZA-DLS76 structure from (a) RPBE-D; (b) grouping of PBE-D, optB86b, and PW91; and (c) grouping of BEEF, RPBE, PBE, PBEsol, optPBE, vdW-DF2, and revPBE-vdW. The functional used to optimize the structure shown for each group is denoted with an asterisk (*). The average distance from the input structure (Δx_{unopt}) is shown in Å for each grouping. See Figure S8 in the Supporting Information for images of the most stable structures in each functional resulting from adsorbate-facilitated restructuring.

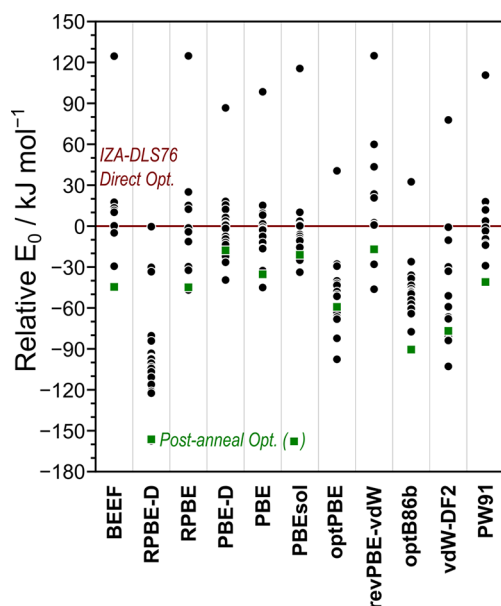


Figure 7. Relative energies of each adsorbate-forced restructured form in each exchange–correlation functional scheme. Circles (●, black) show the relative energies of forms restructured via adsorbates and squares (■, green) show the relative energies of annealed and optimized forms. All energies are relative to the directly optimized IZA-DLS76 structure in each functional.

these metastable states with similar energies would lead to only minor artifacts in calculated energies. In RPBE-D, however, the gap between the most stable structure and the next most stable structure is 35 kJ mol^{-1} . Zeolites are flexible materials, so the presence of multiple local minima with similar energies is expected; however, these structures differ slightly in energy (structures within 20 kJ mol^{-1} differ by $<0.21 \text{ kJ mol}^{-1}$ when normalized per T-site) but significantly in atomic arrangement. These changes in energy, though slight at initial glance, can result in large changes in predictions of catalytic properties. For example, if restructuring occurs for a transition state calculation but not for reactants and products (as shown in Figure 4), the rate constant predicted by DFT calculations would change.

3.3. Annealing To Find Optimal Si-Form Structures.

Simulated annealing using AIMD can overcome restructuring barriers to form more favorable forms of MFI from input structures. Simulated annealing followed by optimization should, in principle, result in the most stable conformation of MFI in each functional if the structure is cooled slowly enough; however, computational restrictions force short annealing times ($<20 \text{ ps}$), and thus, annealed structures were not the global minimum in all cases. These annealing calculations can demonstrate the relative instability of the initial framework. Table 3 shows the energy difference between the annealed-

Table 3. Energy Difference (ΔE_0 , kJ mol^{-1}) between the Annealed and Directly Optimized Structure for Each MFI Source and the DFT Method^a

	IZA-DLS76 (Ads.) ^b	IZA-DLS76	vK-HT-Ortho	Olson-Ortho
BEEF	-45	-45	-4	
RPBE-D	-157	-156		-41
RPBE	-46	-45	-19	
PBE-D	-39	-18		
PBE	-44	-35	-7	-2
PBEsol	-34	-21		-7
optPBE	-98	-59	-1	
revPBE-vdW	-46	-17	-9	
optB86b	-42	-91		
vdW-DF2	-102	-77	-11	
PW91	-41	-41		
average	-63	-55	-5	-5

^aMissing values indicate that annealing did not result in a more stable MFI structure (taken as 0 for averages). ^bEnergy differences for IZA-DLS76 structures obtained through adsorbate-facilitated restructuring (Section 3.2).

optimized structure and the directly optimized input structures. Annealing of the IZA-DLS76 structure resulted in the largest reduction in energy from the directly optimized structure, with an average decrease in energy of 55 kJ mol^{-1} across all DFT methods after annealing. Those functionals that alter the IZA-DLS76 structure least during direct optimization (RPBE-D, optB86b-vdW, optPBE-vdW, and vdW-DF2; $\Delta x_{3\text{N}} < 3.5 \text{ \AA}$ between the optimized and unoptimized structures for each of these functionals) also show the largest decrease in energy from the directly optimized to annealed forms, indicating that the initial atomic positions of IZA-DLS76 are unfavorable across all functionals. Optimization of IZA-DLS76, therefore, leads only to metastable structures which can restructure to minima $18\text{--}156 \text{ kJ mol}^{-1}$ lower in energy without altering framework

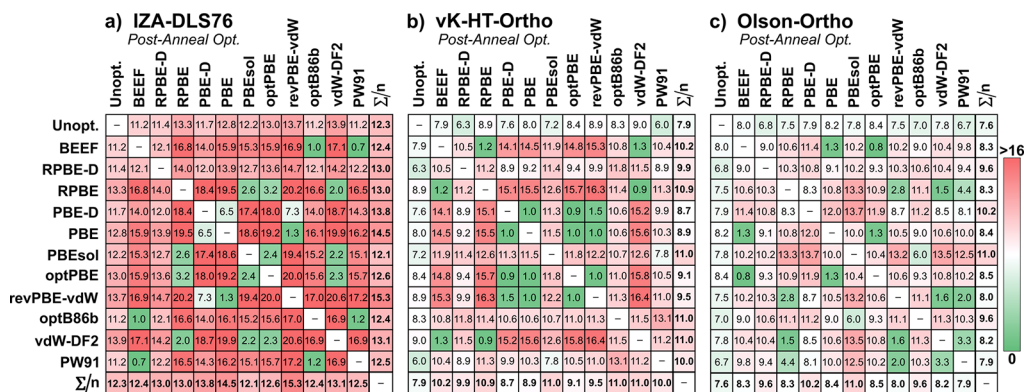


Figure 8. Calculated 3N-dimensional distances between (a) the initial IZA-DLS76 structure, (b) the initial vK-HT-Ortho structure, and (c) the initial Olson-Ortho structure and the structures found by annealing and subsequent optimization in each tested functional. The rightmost column and bottom row (Σ/n) show the average distance between the optimized structure from each functional and those from all other functionals and the unoptimized structure.

connectivity, and initial optimization is insufficient for finding a stable MFI structure.

Annealing the IZA-DLS76 structure leads to very different structures across functionals (Figure 8a). Each of the annealed and optimized structures differ from the input IZA-DLS76 structure by >11 Å, indicating large deviations from the expected structure upon annealing for each functional tested. The distance between the outputs of optB86b, PW91, and BEEF and the distance between the outputs of revPBE-vdW and PBE are <3 Å, indicating that the annealing led to similar structures for these functionals, as is also the case for the RPBE, PBEsol, optPBE, and vdW-DF2 functionals. After annealing and optimization in BEEF, optB86b, and PW91, the well-ordered straight pore becomes distorted, forming two different regimes, where the major axis of the elliptical pore is oriented in two different directions (similar to that shown in Figure 6b,c). This pseudo-sinusoidal pore formation also occurs upon annealing and optimization in vdW-DF2, RPBE, PBEsol, optPBE, PBE, and revPBE-vdW without altering the direction of the major axis of the elliptical pore (Figure 9c,d). Annealing also leads to large distortions in the structure of the sinusoidal pore; the rotational symmetry in the (100) plane is broken in all functionals tested. This is accompanied by twisting in the sinusoidal pore, leading to an elliptical pore shape in all functionals tested, as opposed to the circular and symmetric sinusoidal pore shape of the input IZA-DLS76 structure. The annealed and optimized structures for BEEF and RPBE-D are equivalent to their most stable adsorbate-restructured forms ($\Delta x_{3N} < 3.0$ Å). The random movements associated with AIMD lead to larger deviations from the *Pnma* spacegroup symmetry in these annealed calculations than in the direct-optimization calculations as shown by Δx_{sym} values >8 Å across all functionals for the IZA-DLS76 MFI source, similar to those for adsorbate-facilitated restructured IZA-DLS76 forms ($\Delta x_{\text{sym}} > 8$ Å).

Annealing does not affect the energies of the vK-HT-Ortho nor the Olson-Ortho structures as much as annealing affects IZA-DLS76. On average, the vK-HT-Ortho and Olson-Ortho structures decrease in E_0 by 5 kJ mol^{-1} (Table 3), across all tested functionals. Unlike IZA-DLS76, annealing of the vK-HT-Ortho and Olson-Ortho structures does not universally result in a decrease in E_0 relative to the directly optimized structure, which indicates that the directly optimized structures are stable and near the global minimum. Again, the most extreme change in energy during annealing occurs with RPBE and RPBE-D;

annealing of the vK-HT-Ortho structure results in an E_0 decrease of 19 kJ mol^{-1} with RPBE and annealing of the Olson-Ortho structure results in a decrease in E_0 of 41 kJ mol^{-1} using RPBE-D.

Annealing of vK-HT-Ortho and Olson-Ortho structures does not lead to the same large structural changes as with IZA-DLS76. The distances between the annealed-optimized structures and the unoptimized structures are <8 Å on average for both the vK-HT-Ortho and Olson-Ortho structures, which is ~ 6 Å less than the average distance between the annealed-optimized and unoptimized IZA-DLS76 structures (Figure 8a–c; structures less stable than their directly optimized forms were still included in these figures). As with the optimizations of these structures, annealing leads to more similar structures across functionals than for IZA-DLS76. For example, annealing of the vK-HT-Ortho structure in the PBE, PBE-D, optPBE, and revPBE-vdW functionals leads to the same structure ($\Delta x_{3N} < 3$ Å between each structure). Similarly, annealing and optimization of the Olson-Ortho structure leads to equivalent structures in the PBE, optPBE, and BEEF functionals, indicating more agreement between functionals for these two structures during annealing than with the IZA-DLS76 structure. Annealing the vK-HT-Ortho and Olson-Ortho structures in RPBE-D and optB86b functionals results in structures that are unique to each of those functionals ($\Delta x_{3N} > 3$ Å for all annealed structures in other functionals). While the output structures of annealing in PBE and PBE-D of the vK-HT-Ortho are equivalent, the results of annealing and optimization in RPBE and RPBE-D differ significantly for all three input structures. Furthermore, annealing with the RPBE functional leads to structures that are similar to the outputs of other functionals for the vK-HT-Ortho and Olson-Ortho inputs (vdW-DF2 and BEEF for vK-HT-Ortho and vdW-DF2 and revPBE-vdW for Olson-Ortho), while RPBE-D appears to be an outlier for both. The difference in behavior between RPBE and RPBE-D is much larger than that between PBE and PBE-D during annealing.

Despite the smaller changes in the vK-HT-Ortho and Olson-Ortho structures, annealing these structures still leads to different symmetries than the *Pnma* spacegroup. Distances from symmetry range from 5.2 to 10.4 Å for the annealed vK-HT-Ortho structure, in the PW91 and revPBE-vdW functionals, respectively. Similarly, distances from symmetry range from 5.1 to 10.5 Å for the Olson-Ortho structure, for the PW91 and PBEsol functionals. For each input structure—IZA-DLS76, vK-

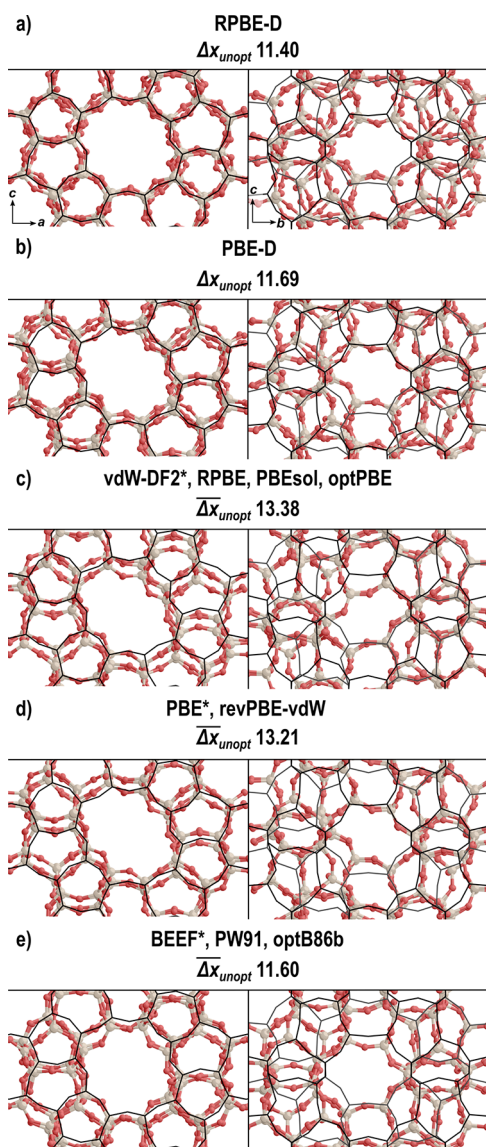


Figure 9. Structures after annealing and optimization restructuring of the IZA-DLS76 structure from (a) RPBE-D; (b) PBE-D; (c) grouping of RPBE, PBEsol, optPBE, and vdW-DF2; (d) PBE and revPBE-vdW; and (e) grouping of BEEF, PW91, and optB86b. The functional used to optimize the structure shown for each group is denoted with an asterisk (*). The average distance from the input structure (Δx_{unopt}) is shown in Å for each grouping. See Figure S5 in the Supporting Information for images of annealed IZA-DLS76 from each functional.

HT-Ortho, and Olson-Ortho—annealing leads to a structure that no longer conforms to the $Pnma$ spacegroup symmetry, regardless of the relative stability of the resulting annealed structures.

Restructuring barriers were analyzed using the NEB method to generate minimum energy pathways between directly optimized MFI structures, annealed structures, and those obtained via adsorbate-facilitated restructuring (Section 3.2). These barriers were less than 85 kJ mol^{-1} in all cases, indicating that these restructuring events are facile at conditions relevant to catalysis.

3.4. Optimization of Unit Cell Parameters. Unit cell parameters for each MFI source structure (Table 1) were optimized constraining unit cell shape and atomic positions (ISIF = 7 in VASP), atomic positions alone (ISIF = 6), and free

of all constraints (ISIF = 3). Unit cell parameter optimizations with constrained atomic positions (ISIF = 6 or 7) led to negligible changes in unit cell volume (<2%) and unit cell vector lengths (<0.09, <0.12, and <0.07 Å change for a , b , and c vectors, respectively) across all functionals (Figure 10). Optimization with or without shape constraints produced nearly identical results, indicating a preference for orthorhombic unit cell geometry when atomic positions were constrained (see Tables S3 and S4, showing unit cell vector lengths and angles, average Si–O bond lengths, and average Si–O–Si angles in the Supporting Information). These constrained unit cell optimizations (performed after atomic coordinate relaxations) do little to stabilize the MFI source files or prevent them from future restructuring during DFT studies.

Optimization of the unit cell parameters with shape relaxation and concomitant atomic relaxation (ISIF = 3), however, yields similar structures regardless of the MFI source structure for functionals without dispersion corrections. These structures (shown in Figures S9–S11 in the Supporting Information) have a nearly circular straight pore, similar to the initial vK-HT-Ortho and Olson-Ortho structures (Figure 1b,c). The unit cell expanded and reached nearly identical unit cell volumes for all three MFI sources for most DFT methods (Figure 10c). RPBE-D, however, decreased the unit cell size, including a severe collapse of the straight pore for the IZA-sourced MFI structure (22% decrease in unit cell volume). These unconstrained unit cell parameter optimizations (ISIF = 3) show large changes in unit cell volume and, as discussed next, significantly decreased potential energies, indicating that these calculations do stabilize the MFI structure against further restructuring during DFT studies. Furthermore, the changes in these unit cell volumes are not predicted by formation energies of the directly optimized MFI structures in each functional (see Table S6 in the Supporting Information).

Dispersion-corrected DFT calculations more accurately capture the properties of silica materials.^{84–87} Dispersion-corrected calculations on MFI, however, tend to underestimate unit cell vector lengths. The RPBE-D functional scheme particularly underestimates the unit cell size of all-silica MFI when optimizing both atomic positions and unit cell parameters: calculated unit cell volumes are up to 22% smaller than those observed experimentally. While unit cell volumes of different MFI models optimized in PBE-D are similar to those found experimentally (Figure 10), the pores of these structures still differ from those observed experimentally (Figures 3, 6, and 9).^{89,90} These alterations in the pore structure may result from overprediction of the Si–O bond lengths with DFT methods.¹¹⁰

3.5. Comparison of Optimization, Annealing, and Adsorbate-Facilitated Restructuring. The directly optimized IZA-DLS76 structure is less stable than directly optimized vK-HT-Ortho and Olson-Ortho structures in all functionals (Figure 11), as also indicated by its relative instability during catalytic studies (adsorption-facilitated restructuring) or through simulated annealing (Table 3). Generally, annealed vK-HT-Ortho and Olson-Ortho structures are also more stable than the annealed IZA-DLS76 structures, and the same trend is observed for the fully unconstrained (ISIF = 3) cell parameter relaxations. The outputs of ISIF = 3 calculations generally yield the lowest potential energies for all DFT methods. These unconstrained unit cell parameter optimizations reduce the energies of the initial structures more in functional schemes that do not account for van der Waals or dispersive interactions (RPBE, PBE, PBEsol, and PW91); unconstrained unit cell

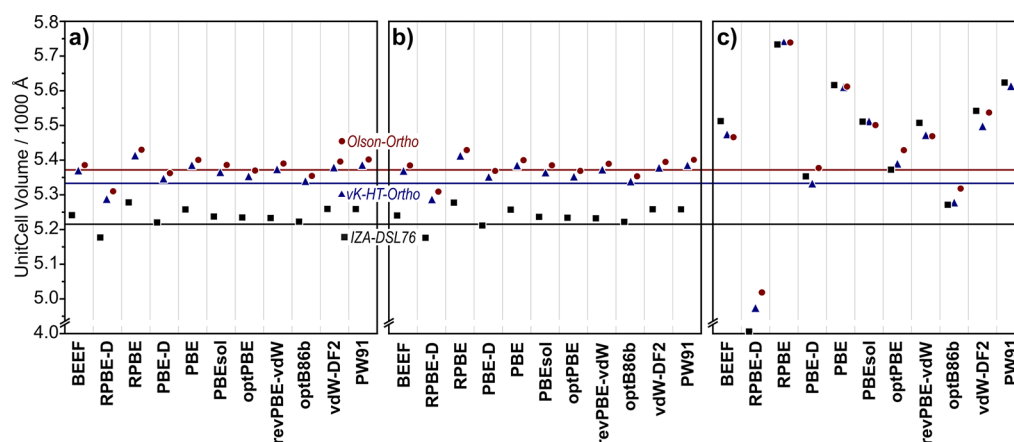


Figure 10. Final volumes of unit cells optimized (a) with the unit cell shape and atomic positions constrained (ISIF = 7), (b) atomic positions constrained (ISIF = 6), and (c) without constraints (ISIF = 3) for IZA-DLS76 (black, ■), vK-HT-Ortho (blue, ▲), Olson-Ortho (red, ●).

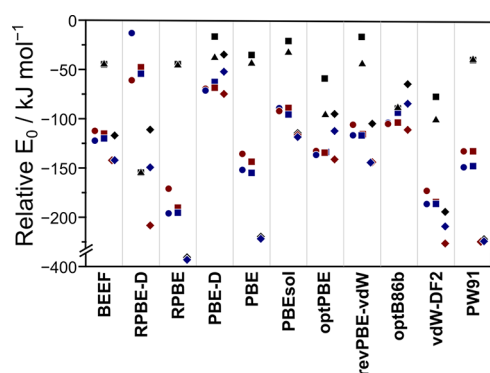


Figure 11. Energies of the most stable structure resulting from direct optimization (●), simulated annealing (■), adsorbate-facilitated restructuring (▲), and unit cell parameter optimization (◆) of IZA-DLS76 (black), vK-HT-Ortho (red), and Olson-Ortho (blue). All energies are relative to the directly optimized IZA-DLS76 structure in each respective functional. Energies shown here were all calculated with an energy cutoff of 800 eV.

parameter optimizations in these functionals also tend to converge to similar pore morphologies regardless of the input (Figures S9–S11 in the Supporting Information). The inclusion of dispersion and van der Waals forces during unit cell optimization appears to affect structure optimization more severely.

Next, we examined the BEA, CHA, and LTA frameworks to determine if similar instabilities of the IZA-sourced structures are observed. The most severe instability in MFI is observed by annealing the IZA-sourced material in the RPBE-D functional scheme with a total energy decrease of 156 kJ mol^{-1} (Table 3), which is 1.63 kJ mol^{-1} per T-site (kJ mol T^{-1}). Identical annealing calculations in RPBE-D were performed for IZA-sourced structures of BEA (64 T-sites per unit cell), CHA (36 T-sites), and LTA (24 T-sites). Annealing these frameworks yielded structures only 0.20, 0.05, and $0.43 \text{ kJ mol T}^{-1}$ for BEA, CHA, and LTA frameworks, respectively, indicating they are significantly more stable than the IZA-sourced MFI structure and have stabilities similar to those of the vK-HT-Ortho and Olson-Ortho MFI source structures.

4. CONCLUSIONS

Three common source structures of the MFI zeolite (IZA-DLS76,⁸⁸ vK-HT-Ortho,⁹⁰ and Olson-Ortho⁸⁹) were optimized

in nine functionals, two of which were tested with and without added dispersive corrections (D3BJ). These DFT methods were applied to these MFI source structures in three ways: direct optimization, adsorption/desorption, and AIMD annealing to examine the structural stability of the catalyst model, the flexibility of the MFI framework, and to compare predicted structures among various methods. Direct optimization of the IZA-DLS76 structure produced a variety of MFI-like frameworks, depending on the DFT method applied, whereas the direct optimizations of the vK-HT-Ortho and Olson-Ortho structures led to nearly identical structures regardless of the DFT method.

Adsorption and desorption of MTO-related species in the IZA-DLS76 structure also revealed instability of Si-form analogues. These alterations of the MFI framework resulted in significant artifacts in the calculation of reaction and activation energies for reactions in MFI that can only be alleviated by the use of a more stable MFI source or by using an already-restructured MFI framework. These adsorbate-facilitated restructuring events of the IZA structure were observed regardless of the DFT method, indicating the unsuitable nature of this material for DFT studies of catalytic and sorptive MFI properties.

The instabilities of all three MFI source structures were examined by simulated annealing using AIMD methods. Once again, the IZA-DLS76 framework was found to be unstable, with energies decreasing by a minimum of 17 kJ mol^{-1} and by an average of 55 kJ mol^{-1} across all DFT methods. Annealing of the vK-HT-Ortho and Olson-Ortho MFI source structures, in contrast, only resulted in more stable structures half the time, and they showed average energy decreases of just 5 kJ mol^{-1} . Annealing of BEA, CHA, and LTA frameworks with RPBE-D—the functional and dispersion-correction scheme with the largest reduction in energy from the directly optimized structure—did not yield structures significantly lower in energy than their directly optimized structures. Direct optimization of the IZA-DLS76 structure is not stable using any DFT method; both adsorption/desorption and simulated annealing results in significant decreases in energy and these energy shifts can lead to artifacts in DFT predictions of adsorption, reaction, and activation energies. Direct optimization of vK-HT-Ortho and Olson-Ortho structures, in contrast, produced much more stable catalyst models suitable for DFT studies.

Unit cell parameter optimizations with fixed atomic coordinates did not result in unit cells with significantly different unit cell vectors or angles (<2% change in unit cell volume). Unit cell parameter optimizations with concomitant atomic relaxation, however, did yield structures significantly more stable than directly optimized structures. The structures resulting from unconstrained unit cell parameter optimizations were not in close agreement with structures found using experimental methods, and unit cell volumes of these optimized structures varied across functionals by >30% of the unit cell volume of vK-HT-Ortho (>1600 Å³). Optimization of unit cell parameters with schemes that included dispersion and van der Waals corrections led to larger variance in the output structures and the energies of output structures; unconstrained unit cell parameter optimization in functionals which do not include dispersive or van der Waals corrections resulted in extremely similar structures regardless of the initial structure.

These results indicate that the IZA-sourced MFI structure is inherently unstable using virtually any DFT method and that the other MFI source structures (from the works of van Koningsveld and Olson) restructure upon initial optimization but are then relatively stable in most DFT methods. The metastable nature of the framework makes it critical to identify the global minimum MFI structure, otherwise restructuring during DFT studies will create large artifacts (up to 160 kJ mol⁻¹) when computing adsorption, reaction, and activation energies using DFT methods. This work describes two techniques (AIMD annealing and fully unconstrained unit cell optimizations) that can mitigate these instabilities leading to appropriate model materials for the study of MFI's catalytic and sorptive properties. Fully unconstrained unit cell optimizations appear to reduce the energies of these structures more than other methods (direct optimization, annealing) which maintain the unit cell size and shape. These unconstrained optimizations, however, can lead to significant changes in the structure of these MFI frameworks with changes in the unit cell volume (average absolute change of 4.6%) especially with the RPBE functional with or without dispersion.

Zeolites are flexible materials, and thus they have many metastable states with low barriers between local minima on their potential energy surfaces. Framework perturbations can occur incidentally (e.g., during reaction studies) or can be forced (e.g., with AIMD annealing) and allow the framework to access a more stable form (a lower-energy local minimum). These shifts in framework energy can cause artifacts, mitigated by restructuring prior to additional catalytic or adsorption studies, at the expense of fidelity with experimentally observed MFI structures. Fully periodic ab initio dynamic studies of adsorptive and catalytic properties overcome these issues by calculating free energies that reflect framework flexibility at appropriate temperatures; however, these methods remain prohibitively expensive for large reaction networks and do not alter unit cell parameters, which themselves have large impacts on MFI energies and stabilities. The first step must then be to identify methods to generate stable ground-state MFI framework structures (annealing or fully unconstrained cell parameter optimizations) for the DFT method of choice and then account for flexibility and entropy using a combination of techniques, including dynamics.

■ ASSOCIATED CONTENT

📄 Supporting Information

The Supporting Information is available free of charge on the ACS Publications website at DOI: 10.1021/acs.jpcc.8b12230.

Information regarding 3N-dimensional distance calculations; analysis of distance cutoffs for determination of unique structures; images of all IZA-DLS76, vK-HT-Ortho and Olson-Ortho structures; and comparisons of directly optimized, annealed, and adsorbate-pathway restructured MFI forms; structural information (average Si–O bond lengths, Si–O–Si angles, unit cell parameters) for structures from each functional (PDF)

Output structures in the POSCAR format for directly optimized structures (IZA-DLS76, vK-HT-Ortho, and Olson Ortho), annealed and optimized structures (IZA-DLS76, vK-HT-Ortho, and Olson Ortho), and those restructured via adsorbates (IZA-DLS76 only) (ZIP)

■ AUTHOR INFORMATION

Corresponding Author

*E-mail: hibbitts@che.ufl.edu.

ORCID

Alexander Hoffman: 0000-0002-1337-9297

David Hibbitts: 0000-0001-8606-7000

Notes

The authors declare no competing financial interest.

■ ACKNOWLEDGMENTS

The authors are grateful for funding from the ACS Petroleum Research Fund New Doctoral Investigation Award (57079-DNIS). This work used the Extreme Science and Engineering Discovery Environment (XSEDE),¹¹¹ which is supported by the National Science Foundation grant number ACI-1548562 through allocation CTS160041. Additional computational resources were provided by the University of Florida Research Computing.

■ REFERENCES

- (1) Davis, M. E. Design for Sieving. *Nature* **1996**, *382*, 583–585.
- (2) Brand, S. K.; Schmidt, J. E.; Deem, M. W.; Daeyaert, F.; Ma, Y.; Terasaki, O.; Orazov, M.; Davis, M. E. Enantiomerically Enriched, Polycrystalline Molecular Sieves. *Proc. Natl. Acad. Sci. U.S.A.* **2017**, *114*, 5101–5106.
- (3) Davis, M. E. Ordered Porous Materials for Emerging Applications. *Nature* **2002**, *417*, 813–821.
- (4) Schmidt, J. E.; Deem, M. W.; Davis, M. E. Synthesis of a Specified, Silica Molecular Sieve by Using Computationally Predicted Organic Structure-directing Agents. *Angew. Chem., Int. Ed. Engl.* **2014**, *53*, 8372–8374.
- (5) Bein, T. Synthesis and Applications of Molecular Sieve Layers and Membranes. *Chem. Mater.* **1996**, *8*, 1636–1653.
- (6) Kissin, Y. V. Chemical Mechanisms of Catalytic Cracking over Solid Acidic Catalysts: Alkanes and Alkenes. *Catal. Rev.* **2001**, *43*, 85–146.
- (7) Janda, A.; Bell, A. T. Effects of Si/Al Ratio on the Distribution of Framework Al and on the Rates of Alkane Monomolecular Cracking and Dehydrogenation in H-MFI. *J. Am. Chem. Soc.* **2013**, *135*, 19193–19207.
- (8) Guo, Y.-H.; Pu, M.; Chen, B.-H.; Cao, F. Theoretical Study on the Cracking Reaction Catalyzed by a Solid Acid with Zeolitic Structure: The Catalytic Cracking of 1-hexene on the Surface of H-ZSM-5. *Appl. Catal., A* **2013**, *455*, 65–70.

- (9) Sadrameli, S. M. Thermal/catalytic Cracking of Liquid Hydrocarbons for the Production of Olefins: A State-of-the-art Review II: Catalytic Cracking Review. *Fuel* **2016**, *173*, 285–297.
- (10) Chen, C.-J.; Rangarajan, S.; Hill, I. M.; Bhan, A. Kinetics and Thermochemistry of C₄–C₆ Olefin Cracking on H-ZSM-5. *ACS Catal.* **2014**, *4*, 2319–2327.
- (11) Van der Mynsbrugge, J.; Janda, A.; Mallikarjun Sharada, S.; Lin, L.-C.; Van Speybroeck, V.; Head-Gordon, M.; Bell, A. T. Theoretical Analysis of the Influence of Pore Geometry on Monomolecular Cracking and Dehydrogenation of n-Butane in Brønsted Acidic Zeolites. *ACS Catal.* **2017**, *7*, 2685–2697.
- (12) Gounder, R. Hydrophobic microporous and mesoporous oxides as Brønsted and Lewis acid catalysts for biomass conversion in liquid water. *Catal. Sci. Technol.* **2014**, *4*, 2877–2886.
- (13) Huber, G. W.; Iborra, S.; Corma, A. Synthesis of Transportation Fuels from Biomass: Chemistry, Catalysts, and Engineering. *Chem. Rev.* **2006**, *106*, 4044–4098.
- (14) Corma, A.; Iborra, S.; Velty, A. Chemical Routes for the Transformation of Biomass into Chemicals. *Chem. Rev.* **2007**, *107*, 2411–2502.
- (15) Jae, J.; Tompsett, G. A.; Foster, A. J.; Hammond, K. D.; Auerbach, S. M.; Lobo, R. F.; Huber, G. W. Investigation into the Shape Selectivity of Zeolite Catalysts for Biomass Conversion. *J. Catal.* **2011**, *279*, 257–268.
- (16) Aho, A.; Kumar, N.; Eränen, K.; Salmi, T.; Hupa, M.; Murzin, D. Y. Catalytic Pyrolysis of Woody Biomass in a Fluidized Bed Reactor: Influence of the Zeolite Structure. *Fuel* **2008**, *87*, 2493–2501.
- (17) French, R.; Czernik, S. Catalytic Pyrolysis of Biomass for Biofuels Production. *Fuel Process. Technol.* **2010**, *91*, 25–32.
- (18) Nikolla, E.; Román-Leshkov, Y.; Moliner, M.; Davis, M. E. "One-Pot" Synthesis of 5-(Hydroxymethyl)furfural from Carbohydrates using Tin-Beta Zeolite. *ACS Catal.* **2011**, *1*, 408–410.
- (19) Jan, O.; Marchand, R.; Anjos, L. C. A.; Seufftelli, G. V. S.; Nikolla, E.; Resende, F. L. P. Hydrolysis of Lignin Using Pd/HZSM-5. *Energy Fuels* **2015**, *29*, 1793–1800.
- (20) Bermejo-Deval, R.; Assary, R. S.; Nikolla, E.; Moliner, M.; Roman-Leshkov, Y.; Hwang, S.-J.; Palsdottir, A.; Silverman, D.; Lobo, R. F.; Curtiss, L. A.; Davis, M. E. Metalloenzyme-like Catalyzed Isomerizations of Sugars by Lewis Acid Zeolites. *Proc. Natl. Acad. Sci. U.S.A.* **2012**, *109*, 9727–9732.
- (21) Gounder, R.; Iglesia, E. The Catalytic Diversity of Zeolites: Confinement and Solvation Effects Within Voids of Molecular Dimensions. *Chem. Commun.* **2013**, *49*, 3491–3509.
- (22) Jones, A. J.; Zones, S. I.; Iglesia, E. Implications of Transition State Confinement Within Small Voids for Acid Catalysis. *J. Phys. Chem. C* **2014**, *118*, 17787–17800.
- (23) Derouane, E. G.; Chang, C. D. Confinement Effects in the Adsorption of Simple Bases by Zeolites. *Micropor. Mesopor. Mat.* **2000**, *35–36*, 425–433.
- (24) Lesthaeghe, D.; Van Speybroeck, V.; Waroquier, M. Theoretical Evaluation of Zeolite Confinement Effects on the Reactivity of Bulky Intermediates. *Phys. Chem. Chem. Phys.* **2009**, *11*, 5222–5226.
- (25) Sastre, G.; Corma, A. The Confinement Effect in Zeolites. *J. Mol. Catal. A: Chem.* **2009**, *305*, 3–7.
- (26) Derouane, E. G. Zeolites as Solid Solvents. *J. Mol. Catal. A: Chem.* **1998**, *134*, 29–45.
- (27) Smit, B.; Maesen, T. L. M. Towards a Molecular Understanding of Shape Selectivity. *Nature* **2008**, *451*, 671–678.
- (28) Haldoupis, E.; Nair, S.; Sholl, D. S. Pore size analysis of >250 000 hypothetical zeolites. *Phys. Chem. Chem. Phys.* **2011**, *13*, 5053–5060.
- (29) First, E. L.; Gounaris, C. E.; Wei, J.; Floudas, C. A. Computational Characterization of Zeolite Porous Networks: An Automated Approach. *Phys. Chem. Chem. Phys.* **2011**, *13*, 17339–17358.
- (30) Baerlocher, C.; McCusker, L. B.; Olson, D. H. *Atlas of Zeolite Framework Types*, 6th ed.; Elsevier, 2007.
- (31) Deem, M. W.; Pophale, R.; Cheeseman, P. A.; Earl, D. J. Computational Discovery of New Zeolite-Like Materials. *J. Phys. Chem. C* **2009**, *113*, 21353–21360.
- (32) Pophale, R.; Cheeseman, P. A.; Deem, M. W. A Database of New Zeolite-like Materials. *Phys. Chem. Chem. Phys.* **2011**, *13*, 12407–12412.
- (33) Tanabe, K.; Hölderich, W. F. Industrial application of solid acid-base catalysts. *Appl. Catal., A* **1999**, *181*, 399–434.
- (34) Ford, M. H.; Auerbach, S. M.; Monson, P. A. Further Studies of a Simple Atomistic Model of Silica: Thermodynamic Stability of Zeolite Frameworks as Silica Polymorphs. *J. Chem. Phys.* **2007**, *126*, 144701.
- (35) Fang, H.; Kamakoti, P.; Zang, J.; Cundy, S.; Paur, C.; Ravikovitch, P. I.; Sholl, D. S. Prediction of CO₂ Adsorption Properties in Zeolites Using Force Fields Derived from Periodic Dispersion-Corrected DFT Calculations. *J. Phys. Chem. C* **2012**, *116*, 10692–10701.
- (36) Fang, H.; Awati, R.; Boufelfel, S.; Ravikovitch, P. I.; Sholl, D. S. First-Principles-Derived Force Fields for CH₄ Adsorption and Diffusion in Siliceous Zeolites. *J. Phys. Chem. C* **2018**.
- (37) Fang, H.; Kamakoti, P.; Ravikovitch, P. I.; Aronson, M.; Paur, C.; Sholl, D. S. First Principles Derived, Transferable Force Fields for CO₂ Adsorption in Na-exchanged Cationic Zeolites. *Phys. Chem. Chem. Phys.* **2013**, *15*, 12882–12894.
- (38) Rozanska, X.; van Santen, R. A.; Demuth, T.; Hutschka, F.; Hafner, J. A Periodic DFT Study of Isobutene Chemisorption in Proton-Exchanged Zeolites: Dependence of Reactivity on the Zeolite Framework Structure. *J. Phys. Chem. B* **2003**, *107*, 1309–1315.
- (39) Zaragoza, I. P.; Martínez-Magadán, J. M.; Santamaria, R.; Dixon, D.; Castro, M. DFT Study of the Interaction of the HZSM-5 Zeolite with the Benzene Molecule. *Int. J. Quantum Chem.* **2000**, *80*, 125–132.
- (40) Siahrostami, S.; Falsig, H.; Beato, P.; Moses, P. G.; Nørskov, J. K.; Studt, F. Exploring Scaling Relations for Chemisorption Energies on Transition-Metal-Exchanged Zeolites ZSM-22 and ZSM-5. *ChemCatChem* **2016**, *8*, 767–772.
- (41) Brogaard, R. Y.; Moses, P. G.; Nørskov, J. K. Modeling van Der Waals Interactions in Zeolites with Periodic DFT: Physisorption of n-Alkanes in ZSM-22. *Catal. Lett.* **2012**, *142*, 1057–1060.
- (42) Nguyen, C. M.; Reyniers, M.-F.; Marin, G. B. Theoretical Study of the Adsorption of C1-C4 Primary Alcohols in H-ZSM-5. *Phys. Chem. Chem. Phys.* **2010**, *12*, 9481–9493.
- (43) Nguyen, C. M.; Reyniers, M.-F.; Marin, G. B. Adsorption thermodynamics of C1-C4 alcohols in H-FAU, H-MOR, H-ZSM-5, and H-ZSM-22. *J. Catal.* **2015**, *322*, 91–103.
- (44) Hernandez-Tamargo, C. E.; Roldan, A.; de Leeuw, N. H. DFT Modeling of the Adsorption of Trimethylphosphine Oxide at the Internal and External Surfaces of Zeolite MFI. *J. Phys. Chem. C* **2016**, *120*, 19097–19106.
- (45) Nystrom, S.; Hoffman, A.; Hibbitts, D. Tuning Brønsted Acid Strength by Altering Site Proximity in CHA Framework Zeolites. *ACS Catal.* **2018**, *8*, 7842–7860.
- (46) Paolucci, C.; Khurana, I.; Parekh, A. A.; Li, S.; Shih, A. J.; Li, H.; Di Iorio, J. R.; Albarracín-Caballero, J. D.; Yezerets, A.; Miller, J. T.; Delgass, W. N.; Ribeiro, F. H.; Schneider, W. F.; Gounder, R. Dynamic multinuclear sites formed by mobilized copper ions in NO_xselective catalytic reduction. *Science* **2017**, *357*, 898–903.
- (47) Paolucci, C.; Parekh, A. A.; Khurana, I.; Di Iorio, J. R.; Li, H.; Albarracín Caballero, J. D.; Shih, A. J.; Anggara, T.; Delgass, W. N.; Miller, J. T.; Ribeiro, F. H.; Gounder, R.; Schneider, W. F. Catalysis in a Cage: Condition-Dependent Speciation and Dynamics of Exchanged Cu Cations in SSZ-13 Zeolites. *J. Am. Chem. Soc.* **2016**, *138*, 6028–6048.
- (48) Jones, A. J.; Carr, R. T.; Zones, S. I.; Iglesia, E. Acid Strength and Solvation in Catalysis by MFI Zeolites and Effects of the Identity, Concentration and Location of Framework Heteroatoms. *J. Catal.* **2014**, *312*, 58–68.
- (49) Jones, A. J.; Iglesia, E. Kinetic, Spectroscopic, and Theoretical Assessment of Associative and Dissociative Methanol Dehydration Routes in Zeolites. *Angew. Chem., Int. Ed. Engl.* **2014**, *53*, 12177–12181.
- (50) Jones, A. J.; Iglesia, E. The Strength of Brønsted Acid Sites in Microporous Aluminosilicates. *ACS Catal.* **2015**, *5*, 5741–5755.

- (51) Sarazen, M. L.; Iglesia, E. Stability of Bound Species During Alkene Reactions on Solid Acids. *Proc. Natl. Acad. Sci. U.S.A.* **2017**, *114*, E3900–E3908.
- (52) Sarazen, M. L.; Dorskocil, E.; Iglesia, E. Catalysis on Solid Acids: Mechanism and Catalyst Descriptors in Oligomerization Reactions of Light Alkenes. *J. Catal.* **2016**, *344*, 553–569.
- (53) Noh, G.; Shi, Z.; Zones, S. I.; Iglesia, E. Isomerization and β -scission Reactions of Alkanes on Bifunctional Metal-acid Catalysts: Consequences of Confinement and Diffusional Constraints on Reactivity and Selectivity. *J. Catal.* **2018**, *368*, 389.
- (54) Tuma, C.; Sauer, J. Quantum Chemical Ab Initio Prediction of Proton Exchange Barriers Between CH₄ and Different H-zeolites. *J. Chem. Phys.* **2015**, *143*, 102810.
- (55) Niwa, M.; Suzuki, K.; Morishita, N.; Sastre, G.; Okumura, K.; Katada, N. Dependence of cracking activity on the Brønsted acidity of Y zeolite: DFT study and experimental confirmation. *Catal. Sci. Technol.* **2013**, *3*, 1919.
- (56) Liu, C.; Li, G.; Hensen, E. J. M.; Pidko, E. A. Relationship Between Acidity and Catalytic Reactivity of Faujasite Zeolite: A Periodic DFT Study. *J. Catal.* **2016**, *344*, 570–577.
- (57) Grajciar, L.; Areán, C. O.; Pulido, A.; Nachtigall, P. Periodic DFT Investigation of the Effect of Aluminium Content on the Properties of the Acid Zeolite H-FER. *Phys. Chem. Chem. Phys.* **2010**, *12*, 1497–1506.
- (58) Moses, P. G.; Nørskov, J. K. Methanol to Dimethyl Ether over ZSM-22: A Periodic Density Functional Theory Study. *ACS Catal.* **2013**, *3*, 735–745.
- (59) Hansen, N.; Kerber, T.; Sauer, J.; Bell, A. T.; Keil, F. J. Quantum Chemical Modeling of Benzene Ethylation over H-ZSM-5 Approaching Chemical Accuracy: a Hybrid MP2:DFT Study. *J. Am. Chem. Soc.* **2010**, *132*, 11525–11538.
- (60) Brogaard, R. Y.; Weckhuysen, B. M.; Nørskov, J. K. Guest-host interactions of arenes in H-ZSM-5 and their impact on methanol-to-hydrocarbons deactivation processes. *J. Catal.* **2013**, *300*, 235–241.
- (61) Tranca, D. C.; Hansen, N.; Swisher, J. A.; Smit, B.; Keil, F. J. Combined Density Functional Theory and Monte Carlo Analysis of Monomolecular Cracking of Light Alkanes Over H-ZSM-5. *J. Phys. Chem. C* **2012**, *116*, 23408–23417.
- (62) Bhan, A.; Joshi, Y. V.; Delgass, W. N.; Thomson, K. T. DFT Investigation of Alkoxide Formation from Olefins in H-ZSM-5. *J. Phys. Chem. B* **2003**, *107*, 10476–10487.
- (63) Alexopoulos, K.; John, M.; Van der Borgh, K.; Galvita, V.; Reyniers, M.-F.; Marin, G. B. DFT-based Microkinetic Modeling of Ethanol Dehydration in H-ZSM-5. *J. Catal.* **2016**, *339*, 173–185.
- (64) Van der Mynsbrugge, J.; De Ridder, J.; Hemelsoet, K.; Waroquier, M.; Van Speybroeck, V. Enthalpy and Entropy Barriers Explain the Effects of Topology on the Kinetics of Zeolite-catalyzed Reactions. *Chemistry* **2013**, *19*, 11568–11576.
- (65) Lesthaeghe, D.; Horré, A.; Waroquier, M.; Marin, G. B.; VanSpeybroeck, V. Theoretical Insights on Methylbenzene Side-chain Growth in ZSM-5 Zeolites for Methanol-to-olefin Conversion. *Chemistry* **2009**, *15*, 10803–10808.
- (66) Hajek, J.; Van der Mynsbrugge, J.; De Wispelaere, K.; Cnudde, P.; Vanduyfhuys, L.; Waroquier, M.; Van Speybroeck, V. On the stability and nature of adsorbed pentene in Brønsted acid zeolite H-ZSM-5 at 323 K. *J. Catal.* **2016**, *340*, 227–235.
- (67) Martinez-Espin, J. S.; De Wispelaere, K.; Westgård Erichsen, M.; Svelle, S.; Janssens, T. V. W.; Van Speybroeck, V.; Beato, P.; Olsbye, U. Benzene Co-reaction with Methanol and Dimethyl Ether over Zeolite and Zeotype Catalysts: Evidence of Parallel Reaction Paths to Toluene and Diphenylmethane. *J. Catal.* **2017**, *349*, 136–148.
- (68) Van der Mynsbrugge, J.; Visur, M.; Olsbye, U.; Beato, P.; Bjørgen, M.; Van Speybroeck, V.; Svelle, S. Methylation of Benzene by Methanol: Single-site Kinetics over H-ZSM-5 and H-beta Zeolite Catalysts. *J. Catal.* **2012**, *292*, 201–212.
- (69) Ghorbanpour, A.; Rimer, J. D.; Grabow, L. C. Periodic, vdW-corrected Density Functional Theory Investigation of the Effect of Al Siting in H-ZSM-5 on Chemisorption Properties and Site-specific Acidity. *Catal. Commun.* **2014**, *52*, 98–102.
- (70) Ghorbanpour, A.; Rimer, J. D.; Grabow, L. C. Computational Assessment of the Dominant Factors Governing the Mechanism of Methanol Dehydration over H-ZSM-5 with Heterogeneous Aluminum Distribution. *ACS Catal.* **2016**, *6*, 2287–2298.
- (71) Almutairi, S. M. T.; Mezari, B.; Magusin, P. C. M. M.; Pidko, E. A.; Hensen, E. J. M. Structure and Reactivity of Zn-Modified ZSM-5 Zeolites: The Importance of Clustered Cationic Zn Complexes. *ACS Catal.* **2011**, *2*, 71–83.
- (72) Li, G.; Pidko, E. A.; van Santen, R. A.; Feng, Z.; Li, C.; Hensen, E. J. M. Stability and Reactivity of Active Sites for Direct Benzene Oxidation to Phenol in Fe/ZSM-5: A Comprehensive Periodic DFT Study. *J. Catal.* **2011**, *284*, 194–206.
- (73) Mazar, M. N.; Al-Hashimi, S.; Cococcioni, M.; Bhan, A. β -Scission of Olefins on Acidic Zeolites: A Periodic PBE-D Study in H-ZSM-5. *J. Phys. Chem. C* **2013**, *117*, 23609–23620.
- (74) Zhai, D.; Liu, Y.; Zheng, H.; Zhao, L.; Gao, J.; Xu, C.; Shen, B. A first-principles evaluation of the stability, accessibility, and strength of Brønsted acid sites in zeolites. *J. Catal.* **2017**, *352*, 627–637.
- (75) Hernandez-Tamargo, C. E.; Roldan, A.; de Leeuw, N. H. Density Functional Theory Study of the Zeolite-mediated Tautomerization of Phenol and Catechol. *Molecular Catalysis* **2017**, *433*, 334–345.
- (76) Gumidyala, A.; Wang, B.; Crossley, S. Direct carbon-carbon coupling of furanics with acetic acid over Brønsted zeolites. *Sci. Adv.* **2016**, *2*, e1601072.
- (77) Svelle, S.; Tuma, C.; Rozanska, X.; Kerber, T.; Sauer, J. Quantum Chemical Modeling of Zeolite-catalyzed Methylation Reactions: Toward Chemical Accuracy for Barriers. *J. Am. Chem. Soc.* **2009**, *131*, 816–825.
- (78) Noh, G.; Zones, S. I.; Iglesia, E. Consequences of Acid Strength and Diffusional Constraints for Alkane Isomerization and β -Scission Turnover Rates and Selectivities on Bifunctional Metal-Acid Catalysts. *J. Phys. Chem. C* **2018**, *122*, 25475.
- (79) Lee, K.; Murray, É. D.; Kong, L.; Lundqvist, B. I.; Langreth, D. C. Higher-accuracy van Der Waals Density Functional. *Phys. Rev. B: Condens. Matter Mater. Phys.* **2010**, *82*, No. 081101(R).
- (80) Román-Pérez, G.; Soler, J. M. Efficient Implementation of a van Der Waals Density Functional: Application to Double-wall Carbon Nanotubes. *Phys. Rev. Lett.* **2009**, *103*, 096102.
- (81) Perdew, J. P.; Burke, K.; Ernzerhof, M. Generalized Gradient Approximation Made Simple. *Phys. Rev. Lett.* **1996**, *77*, 3865–3868.
- (82) Grimme, S.; Ehrlich, S.; Goerigk, L. Effect of the Damping Function in Dispersion Corrected Density Functional Theory. *J. Comput. Chem.* **2011**, *32*, 1456–1465.
- (83) Grimme, S.; Antony, J.; Ehrlich, S.; Krieg, H. A Consistent and Accurate Ab Initio Parametrization of Density Functional Dispersion Correction (DFT-D) for the 94 Elements H-Pu. *J. Chem. Phys.* **2010**, *132*, 154104.
- (84) Román-Román, E. I.; Zicovich-Wilson, C. M. The role of long-range van der Waals forces in the relative stability of SiO₂-zeolites. *Chem. Phys. Lett.* **2015**, *619*, 109–114.
- (85) Hay, H.; Ferlat, G.; Casula, M.; Seitsonen, A. P.; Mauri, F. Dispersion Effects in SiO₂ Polymorphs: An ab Initio Study. *Phys. Rev. B: Condens. Matter Mater. Phys.* **2015**, *92*, 144111.
- (86) Fischer, M.; Angel, R. J. Accurate Structures and Energetics of Neutral-framework Zeotypes from Dispersion-corrected DFT Calculations. *J. Chem. Phys.* **2017**, *146*, 174111.
- (87) Fischer, M.; Evers, F. O.; Formalik, F.; Olejniczak, A. Benchmarking DFT-GGA Calculations for the Structure Optimisation of Neutral-framework Zeotypes. *Theor. Chem. Acc.* **2016**, *135*, 257.
- (88) Baerlocher, C.; McCusker, L. B. Database of Zeolite Structures. <http://www.iza-structure.org/databases>, 2013 (accessed January 5, 2017).
- (89) Olson, D. H.; Kokotailo, G. T.; Lawton, S. L.; Meier, W. M. Crystal Structure and Structure-related Properties of ZSM-5. *J. Phys. Chem.* **1981**, *85*, 2238–2243.
- (90) van Koningsveld, H. High-temperature (350 K) Orthorhombic Framework Structure of Zeolite H-ZSM-5. *Acta Crystallogr. B Struct. Sci.* **1990**, *46*, 731–735.

- (91) Kresse, G.; Furthmüller, J. Efficiency of Ab-initio Total Energy Calculations for Metals and Semiconductors Using a Plane-wave Basis Set. *Comp. Mater. Sci.* **1996**, *6*, 15–50.
- (92) Kresse, G.; Furthmüller, J. Efficient iterative schemes for ab initio total-energy calculations using a plane-wave basis set. *Phys. Rev. B: Condens. Matter Mater. Phys.* **1996**, *54*, 11169–11186.
- (93) Kresse, G.; Hafner, J. Ab initio molecular-dynamics simulation of the liquid-metal-amorphous-semiconductor transition in germanium. *Phys. Rev. B: Condens. Matter Mater. Phys.* **1994**, *49*, 14251–14269.
- (94) Kresse, G.; Hafner, J. Ab initio molecular dynamics for liquid metals. *Phys. Rev. B: Condens. Matter Mater. Phys.* **1993**, *47*, 558–561.
- (95) Blöchl, P. E. Projector Augmented-wave Method. *Phys. Rev. B: Condens. Matter Mater. Phys.* **1994**, *50*, 17953–17979.
- (96) Hammer, B.; Hansen, L. B.; Nørskov, J. K. Improved Adsorption Energetics Within Density-functional Theory Using Revised Perdew-Burke-Ernzerhof Functionals. *Phys. Rev. B: Condens. Matter Mater. Phys.* **1999**, *59*, 7413–7421.
- (97) Klimeš, J.; Bowler, D. R.; Michaelides, A. Van Der Waals Density Functionals Applied to Solids. *Phys. Rev. B: Condens. Matter Mater. Phys.* **2011**, *83*, 195131.
- (98) Klimeš, J.; Bowler, D. R.; Michaelides, A. Chemical Accuracy for the van Der Waals Density Functional. *J Phys Condens Matter* **2010**, *22*, 022201.
- (99) Perdew, J. P.; Wang, Y. Accurate and Simple Analytic Representation of the Electron-gas Correlation Energy. *Phys. Rev. B: Condens. Matter Mater. Phys.* **1992**, *45*, 13244–13249.
- (100) Perdew, J. P.; Chevary, J. A.; Vosko, S. H.; Jackson, K. A.; Pederson, M. R.; Singh, D. J.; Fiolhais, C. Atoms, Molecules, Solids, and Surfaces: Applications of the Generalized Gradient Approximation for Exchange and Correlation. *Phys. Rev. B: Condens. Matter Mater. Phys.* **1992**, *46*, 6671–6687.
- (101) Dion, M.; Rydberg, H.; Schröder, E.; Langreth, D. C.; Lundqvist, B. I. Van Der Waals Density Functional for General Geometries. *Phys. Rev. Lett.* **2004**, *92*, 246401.
- (102) Thonhauser, T.; Cooper, V. R.; Li, S.; Puzder, A.; Hyldgaard, P.; Langreth, D. C. Van Der Waals Density Functional: Self-consistent Potential and the Nature of the van Der Waals Bond. *Phys. Rev. B: Condens. Matter Mater. Phys.* **2007**, *76*, 125112.
- (103) Perdew, J. P.; Ruzsinszky, A.; Csonka, G. I.; Vydrov, O. A.; Scuseria, G. E.; Constantin, L. A.; Zhou, X.; Burke, K. Restoring the Density-gradient Expansion for Exchange in Solids and Surfaces. *Phys. Rev. Lett.* **2008**, *100*, 136406.
- (104) Csonka, G. I.; Perdew, J. P.; Ruzsinszky, A.; Philipsen, P. H. T.; Lebègue, S.; Paier, J.; Vydrov, O. A.; Ángyán, J. G. Assessing the Performance of Recent Density Functionals for Bulk Solids. *Phys. Rev. B: Condens. Matter Mater. Phys.* **2009**, *79*. DOI: [10.1103/physrevb.79.155107](https://doi.org/10.1103/physrevb.79.155107)
- (105) Wellendorff, J.; Lundgaard, K. T.; Møgelhøj, A.; Petzold, V.; Landis, D. D.; Nørskov, J. K.; Bligaard, T.; Jacobsen, K. W. Density Functionals for Surface Science: Exchange-correlation Model Development with Bayesian Error Estimation. *Phys. Rev. B: Condens. Matter Mater. Phys.* **2012**, *85*, 235149.
- (106) Yang, K.; Zheng, J.; Zhao, Y.; Truhlar, D. G. Tests of the RPBE, revPBE, τ -HCTHhyb, ω B97X-D, and MOHLYP density functional approximations and 29 others against representative databases for diverse bond energies and barrier heights in catalysis. *J. Chem. Phys.* **2010**, *132*, 164117.
- (107) Bucko, T.; Hafner, J.; Benko, L. Adsorption and vibrational spectroscopy of CO on mordenite: Ab initio density-functional study. *J Phys Chem B* **2005**, *109*, 7345–7357.
- (108) Henkelman, G.; Jónsson, H. Improved Tangent Estimate in the Nudged Elastic Band Method for Finding Minimum Energy Paths and Saddle Points. *J. Chem. Phys.* **2000**, *113*, 9978–9985.
- (109) Jónsson, H.; Mills, G.; Jacobsen, K. W. Nudged Elastic Band Method for Finding Minimum Energy Paths of Transitions. In *Classical and Quantum Dynamics in Condensed Phase Simulations*; Berne, B. J., Ciccotti, G., Coker, D. F., Eds.; World Scientific, 1998; pp 385–404.
- (110) Demuth, T.; Jeanvoine, Y.; Hafner, J.; Ángyán, J. G. Polymorphism in Silica Studied in the Local Density and Generalized-gradient Approximations. *J. Phys.: Condens. Matter* **1999**, *11*, 3833–3874.
- (111) Towns, J.; Cockerill, T.; Dahan, M.; Foster, I.; Gaither, K.; Grimshaw, A.; Hazlewood, V.; Lathrop, S.; Lifka, D.; Peterson, G. D.; Roskies, R.; Scott, J. R.; Wilkens-Diehr, N. XSEDE: Accelerating Scientific Discovery. *Comput. Sci. Eng.* **2014**, *16*, 62–74.